Active and passive spectroscopic imaging in the DIII-D tokamak

2010 Plasma Phys. Control. Fusion 52 045006

(http://iopscience.iop.org/0741-3335/52/4/045006)

Plasma Phys. Control. Fusion **52** (2010) 045006 (22pp) doi:10.1088/0741-3335/52/4/045006

Active and passive spectroscopic imaging in the DIII-D tokamak

M A Van Zeeland[1], J H Yu[2], N H Brooks[1], W W Heidbrink[3], K H Burrell[1], R J Groebner[1], A W Hyatt[1], T C Luce[1], N Pablant[2], W M Solomon[4], M R Wade[1]

[1] General Atomics, PO Box 85608 San Diego, CA 92186-5608, USA
[2] University of California-San Diego, 9500 Gilman Drive, La Jolla, CA 92093, USA
[3] University of California-Irvine, 4129 Frederick Reines Hall, Irvine, CA 92697, USA
[4] Princeton Plasma Physics Laboratory, PO Box 451, Princeton, NJ 08543, USA

E-mail: vanzeeland@fusion.gat.com

Received 10 September 2009, in final form 30 November 2009
Published 5 March 2010
Online at stacks.iop.org/PPCF/52/045006

Abstract
Wide-angle, 2D imaging of Doppler-shifted, Balmer alpha (D_α) emission from high energy injected neutrals, charge exchange recombination (CER) emission from neutral beam interaction with thermal ions and fully stripped impurity ions and visible bremsstrahlung (VB) from the core of DIII-D plasmas has been carried out. Narrowband interference filters were used to isolate the specific wavelength ranges of visible radiation for detection by a tangentially viewing, fast-framing camera. Measurements of the D_α emission from fast neutrals injected into the plasma from the low field side reveal the vertical distribution of the beam, its divergence and the variation in its radial penetration with density. Modeling of this emission using both a full Monte Carlo collisional radiative code as well as a simple beam attenuation code coupled to Atomic Data and Analysis Structure emissivity lookup tables yields qualitative agreement, however the absolute magnitudes of the emissivities in the predicted distribution are larger than those measured. Active measurements of carbon CER brightness are in agreement with those made independently along the beam midplane using DIII-D's multichordal, CER spectrometer system, confirming the potential of this technique for obtaining 2D profiles of impurity density. Passive imaging of VB, which can be inverted to obtain local emissivity profiles, is compared with measurements from both a calibrated filter/photomultiplier array and the standard multichordal CER spectrometer system.

(Some figures in this article are in colour only in the electronic version)

1. Introduction

Through recent breakthroughs in the use of fast-framing camera technology, visible imaging has proven to be an extremely powerful tool for diagnosing *core* tokamak plasma conditions and phenomena. Two such applications from DIII-D have been reported recently. Bremsstrahlung imaging [1], which extrapolates well to future high density devices, has provided wide field-of-view measurements of core MHD [2–4], and imaging of Doppler-shifted D_α from re-neutralized beam ions has provided high spatial resolution fast ion profile information [5, 6]. Further developments, such as those presented in this paper as well as others being developed elsewhere [7–10], are helping to provide detailed 2D measurements of neutral beam deposition and core kinetic profiles of everything ranging from carbon impurity density to electron density, temperature and flow velocity. Fortuitously, these high resolution measurements of phenomena and equilibrium parameters are becoming available just in time for validation of the increasingly detailed codes required to make believable predictions for future devices such as ITER.

The application of visible light spectroscopy to fusion plasmas is well established for measuring core tokamak plasma parameters as well as fluctuation profiles, of both coherent and incoherent character [11, 12]. Traditionally, these types of measurements are carried out using individual sightline systems often coupled to spectrometers; while high spectroscopic resolution is possible with this approach, combining that resolution with detailed 2D spatial coverage is costly and difficult to implement. Spectroscopic imaging offers a trade-off in wavelength resolution for spatial resolution and, with the advent of deep memory, large dynamic range, fast-framing (>100 kHz) cameras, often fast imaging comes with enhanced temporal resolution. Spectroscopic imaging as discussed here uses a narrowband interference filter combined with a fast-framing camera to obtain 2D, wide field-of-view (FOV) images of the intensity in an isolated wavelength band of interest. Recently, innovations on this simple approach have been developed that, through essentially interferometric techniques, greatly increase the obtainable spectroscopic information—so-called 'coherence imaging' [7–10].

This paper discusses the application of spectroscopic imaging to active and passive emission sources, i.e. those with and without, respectively, a source of injected neutrals in DIII-D deuterium L-mode plasmas. The source of injected neutrals is an 80 keV neutral beam used for heating. The two main active emission sources discussed here are D_α radiation ($\lambda_{D_\alpha} = 656.1$ nm) from deuterium neutrals transitioning from the $n = 3$ state, both injected in the beam and created through charge exchange with thermals, as well as carbon charge exchange recombination (CER) emission ($\lambda_c = 529.05$ nm). Similar active measurements were made previously of edge plasmas in DIII-D using lithium beam fluorescence [13]. The carbon CER emission results from charge exchange events between fully stripped carbon impurity ions and fast neutrals in the beam. Measurements of emission from injected neutrals reveal the full vertical distribution of high energy neutrals, their divergence and the 2D attenuation variation with density. Modeling of this emission using both a full Monte Carlo collisional radiative code as well as a simple beam attenuation code coupled to Atomic Data and Analysis Structure (ADAS) emissivity lookup tables yields qualitative agreement, however the absolute magnitudes of the emissivities in the predicted distribution are larger than those measured [15, 16]. Camera measurements of impurity CER brightness are in agreement with those made independently using DIII-D's multichordal CER spectrometer, showing the potential of this technique for obtaining 2D, wide FOV measurements of impurity density profiles. Passive imaging of visible bremsstrahlung (VB) is also discussed and comparison with both a calibrated filter/photodetector array and spectrometer array is made. The obtained VB profiles are inverted to obtain local emissivity profiles. Both CER and VB measurements

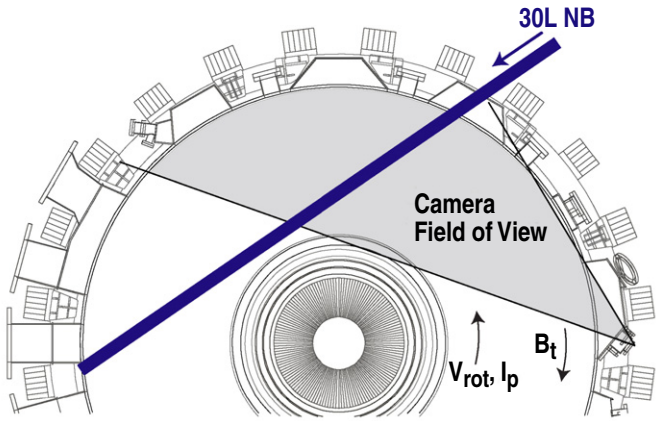

Figure 1. Plan view of DIII-D tokamak showing the camera viewing region in gray. Arrows indicate direction of toroidal field (B_t), plasma current (I_p), toroidal rotation (v_{rot}) and neutral beam injection. The $1/e$ width of the 30L neutral beam is approximately to scale.

are used to obtain *in situ* absolute camera intensity calibrations through comparison with the well-calibrated DIII-D CER spectrometer system.

2. Experimental setup

Figure 1 shows a plan view of the DIII-D tokamak midplane, as well as the viewable region of the fast-framing camera (shaded gray). The semi-tangential view spans the plasma volume from the inner wall on the high field side (HFS) to the outer wall on the low field side (LFS). The spatial resolution of the detector is 384×256 pixels, with 1 pixel mapping to a rectangular region between 0.05 and 0.2 cm^2 at the point of tangency, the exact size depending on the location within the FOV. The number of usable pixels depends on the camera frame rate which varied between 100 and 900 frames s^{-1} for the study presented here. The camera itself is capable of frame rates up to 120 k frames s^{-1}. Taking advantage of this large bandwidth and dynamic range the same camera has been used to provide detailed measurements of tearing modes through imaging of VB emission [2, 3] as well as fast transient events such as edge localized modes (ELMs) [14] through cold edge D_α imaging. As an active diagnostic, the fast-framing camera has been used recently for imaging of fast ion D_α (FIDA) emission to obtain 2D fast ion profile information [5]. The $E_b = 80$ keV injected neutral beam that makes active diagnostics possible is shown in figure 1, along with the direction of toroidal field (B_T), plasma current (I_p) and toroidal rotation (v_{rot}).

One artifact of the measurement apparatus that had to be considered is that mechanical vignetting significantly attenuates signal levels for pixels away from the central region. This attenuation factor has been measured using a uniform intensity light source and an approximate fit is given by

$$V = \exp\left[-\left(\frac{[(x-x_o)^2 + (y-y_o)^2]^{1/2}}{A}\right)^B\right], \quad (1)$$

where $x(y)$ is the horizontal(vertical) pixel, $x_o = 199.3$, $y_o = 119.9$, $A = 138.8$ and $B = 2.61$. Pixel intensities near the inner and outer wall are attenuated by approximately 80%–90% from what would be measured in the absence of this effect.

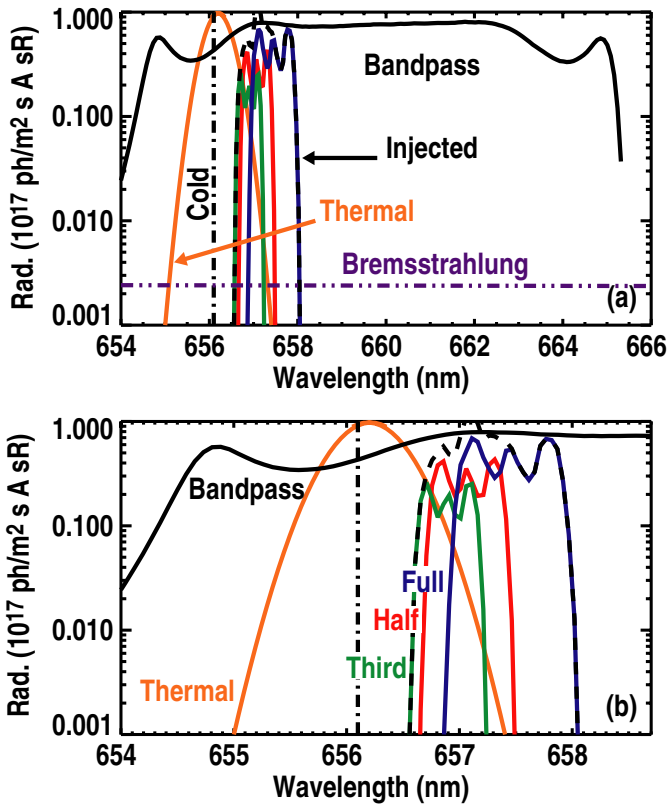

Figure 2. Monte Carlo collisional radiative modeling calculation for D_α spectrum observed by camera sightline intersecting the 30L neutral beam at $R = 2.01$ m, $z = 0$ m, where $n_e \approx 2\times10^{13}$ cm^{-3}, $T_e = 0.5$ keV, $Z_{eff} = 1.2$. Corresponds to predicted spectrum for $R = 2.01$ m, $z = 0$ m in figure 4(*b*). Normal incidence bandpass filter transmission function is overlaid (solid black) as well as location of cold D_α edge line (dash–dot) and line-integrated bremsstrahlung emission (dash–dot–dot). (*b*) Enlarged region of panel (*a*) showing more clearly the full (blue), half (red) and third (green) energy beam emission contributions as well as that from thermal charge exchange events (orange).

3. Active imaging

3.1. Imaging of injected neutral emission

The camera images light with wavelengths spanning the entire visible range which can be from any variety of sources. As discussed in the introduction, to restrict the light to that about D_α, a narrowband interference filter was used that has an approximate normal incidence passband centered at $\lambda_c = 660$ nm with an approximate full-width to the $1/e$ transmission points of 10 nm. This spectral region envelopes the D_α line ($\lambda_{D_\alpha} = 656.1$ nm) asymmetrically from the blue side to several nanometers on the red side. The bandpass is shown in figure 2 along with the primary sources of emission in this region. The theoretical spectra shown are calculated by a collisional radiative modeling code designed to simulate FIDA measurements [15, 16] and will be discussed further in section 3.2. The primary sources of emission in this wavelength region are injected neutrals, thermal neutrals formed by charge exchange events with plasma deuterons, VB emission, the cold edge neutrals and reneutrals formed by charge exchange

events with circulating fast ions (FIDA). The FIDA emission spectrum is not shown since its contribution is negligible for the measurements made here. Experimentally, three different beam energy components are present in the injected neutral population, the full (80 keV), half (80/2 keV) and third (80/3 keV), which are formed because the positive ion sources of deuterium produce three molecular ion species: D^+, D_2^+ and D_3^+. Due to their different masses, the three molecular species are accelerated to three different velocities before passing through the neutralizer and forming a single atomic species of D^0 with three different energy components [21]. At full operating voltage, the relative power in the full, half and third energy components is approximately 73 : 20 : 7, respectively. The individual contribution of each of these is shown in figure 2. Other sources of emission in this range not shown in figure 2 are the two C II lines 658.3 and 657.8 nm that are localized to the edge region and are present because of DIII-D's carbon tile walls—more on carbon emission measurements will be discussed in section 3.4. The relative magnitudes of these different contributions are, of course, very dependent on the sightline and plasma parameters. The radiances given in figure 2 correspond to a midplane sightline intersection with the 30L neutral beam at $R = 2.01$ cm, where $n_e \approx 2 \times 10^{13}$ cm^{-3}, $T_e = 0.5$ keV, $Z_{eff} = 1.2$.

Although it is planned to install a spectrometer in line with the camera FOV, no such spectrometer channel exists to date. Measurements have been made, however, of the 30L neutral beam in the D_α wavelength range with the purpose of obtaining an internal magnetic field diagnostic based on the intensity and spacing of the motional Stark multiplet [22]. Figure 2 of [22] is an example spectrum obtained by this diagnostic that displays many of the features shown in figure 2, with the exception that the beam emission is observed to be blue shifted due to a beam view opposite to that of the camera. All three beam components are clearly represented in figure 2 of [22] as well as a uniform bremsstrahlung background and thermal charge exchange emission. The thermal charge exchange emission (pixels ≈150–250) is truncated, however, one can see that its level is, at minimum, of the same order as the beam emission. Work is currently underway to make a direct comparison between data from this diagnostic as well as a similar system to simulated spectra like that shown in figure 2 [23].

The D_α filter used was not chosen specifically for injected neutrals imaging and, though its bandwidth is fairly wide, proves useful given the variation of the Doppler shift across the FOV. The injected full energy component (80 keV deuterium) D_α observed wavelength increases from 656.1 nm on the outboard midplane to 659.6 nm on the inboard midplane whereas that of the third energy component varies from 656.1 to 658.1 due to the varied intersection angle of each LOS with the neutral beam. Additionally, each of these lines is broadened by Stark splitting as shown in figure 2, requiring an even broader wavelength range. Another geometrical effect dictating the use of a wide filter for imaging is the fact that not all rays across the FOV pass through the filter at normal incidence. This effect causes a blue shift of the filter passband according to $\lambda_c' = \lambda_c\sqrt{1 - \sin(\theta)^2/n_{eff}^2}$, where $n_{eff} = 2.05$ is the effective index of refraction for the filter and the angles are up to ≈5° near the edges of the FOV.

Figure 3 shows typical false color 384 × 256 pixel images taken with the D_α filter from figure 2, where figures 3(*a*) and (*b*) are with the imaged neutral beam ON and OFF and figure 3(*c*) is the difference of the two. Beam modulation allows separation of the active signal contributions from the passive ones. The difference image (figure 3(*c*)) is the active D_α emission which is from injected neutrals and ions which have undergone charge exchange events with either the injected neutrals (direct) or other neutrals formed from these charge exchange events (halo). Unfortunately, due to the filter passband and beam injection geometry, the two contributions cannot be completely isolated. Modeling, which will be discussed in the next section, indicates that between 60% and 90% (depending on parameters and position)

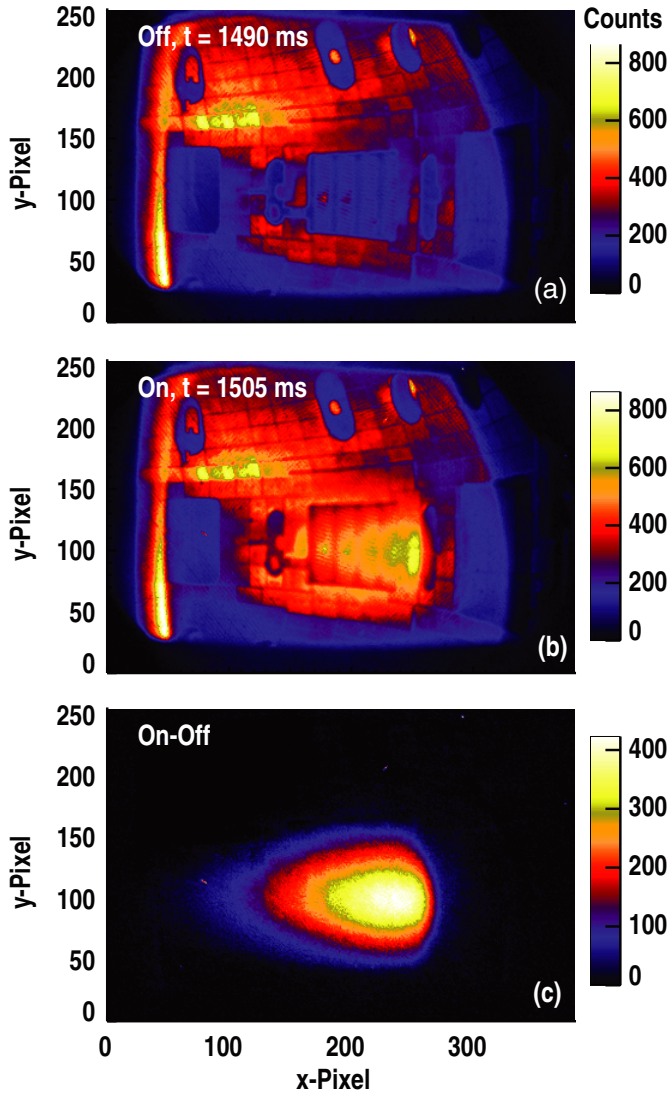

Figure 3. D_α imaging data from DIII-D discharge 135851 showing (*a*) 30L beam off, (*b*) 30L beam on, (*c*) panel (*b*) through panel (*a*). Camera sampling rate was 900 frames s^{-1} and exposure time was 1.1 ms. Approximately the top ten and bottom 30 rows of pixels are dark due to mechanical clipping of the FOV. 'Counts' are out of 4096 set by camera dynamic range of 12-bits.

of the measured signal is due to beam emission. In both images 3(*a*) and (*b*), edge emission from cold D_α and the C II lines mentioned above is obvious. In the difference image these dc contributions are reduced to the sub-percent level. The efficacy of background subtraction is key to active imaging and is most effective in L-mode plasmas, such as those presented here, due to the lack of ELMs and other transient events that can cause a non-stationary background from frame to frame. It should be pointed out, however, that active imaging, where beam modulation was used to recover the active signal contribution, has been carried out in H-mode plasmas; one example is the FIDA imaging study presented in [5]. For imaging using filters which include contributions from the cold D_α edge emission, background subtraction

in the presence of ELMs is best carried out using frames that are obtained between ELMs bursts.

The local D_α emissivity of high energy collisionally excited injected neutrals is given by $E_{D\alpha} = F_3(E_b, n_e, T_e, T_i, Z_{eff})A_{32}n_o$, where F_3 is the local fractional population of deuterium neutrals in the $n = 3$ state (a function of beam energy (E_b), electron density (n_e), electron temperature (T_e), ion temperature (T_i) and Z_{eff}), $A_{32} = 4.4\times10^7\ s^{-1}$ is the Einstein spontaneous coefficient of emission and n_o is the injected neutral density [12, 18, 19]. For the relatively low plasma ion temperatures here (<4 keV), the fractional excited state population is primarily a function of n_e, T_e and E_b, the latter being fixed at $\approx$40 keV amu^{-1} for the full energy component [18, 19]. The total observed emission is a sum over the contributions from the full, the half and the third energy components.

The local neutral density in the beam plume also depends sensitively on n_e and T_e as well as somewhat on Z_{eff}, since the beam is injected from the outboard midplane and is attenuated by ions and electrons. The injected neutral attenuation increases rapidly with plasma density, a dependence illustrated dramatically in the sequence of images shown in figure 4. Figures 4((*a*)–(*e*)) show the change in active D_α signal as plasma density increases, where the line-averaged density is given in each panel. Figure 4(*f*) shows the temporal evolution of the line-averaged density, beam modulation and evolution of the raw signal level at $(R, z) \approx (1.87, 0.0)$. The images shown are plotted at the R, z intersection point of each pixel's sightline with the injected neutral beam and equally spaced contours of ρ (square root of normalized toroidal flux) from 0.1 to 1.0 at those R, z locations are overlaid. The dashed horizontal lines represent the approximate vertical extent of the injected neutral beam.

3.2. Modeling of injected neutral images

The measured emission profiles shown in figure 4 are a result of several factors that, in an approximate sense, can be modeled separately; they are the attenuation of the beam neutrals due to charge exchange and ionization [$N_A(R, z)$], the vertical neutral profile set by the source [$N_s(R, z)$] and the local excited state fraction of neutrals in the $n = 3$ state. For simplicity, and to gain a qualitative understanding of the primary effects determining the overall 2D spatial emission profile, we neglect momentarily the neutrals created through thermal charge exchange. The neutral density of each energy beam species can be defined as $n_o = n_i N_A(R, z)N_s(R, z)$, where n_i is the peak neutral density of each species outside of the plasma and N_A and N_s range from 0 to 1. If divergence is neglected, the vertical neutral profile is only a function of z. These different factors are separately illustrated in figure 5: where the attenuation factor for full energy neutrals [$N_A(R, z)$] propagating ballistically on horizontal trajectories is depicted in figure 5(*a*), the beam neutralizer-induced, vertical neutral footprint [$N_s(R, z)$] in figure 5(*b*) and the local D_α emissivity of full energy neutrals is given in figure 5(*c*). Each profile is shown across the camera FOV at the location of the neutral beam/sightline intersection. The neutral attenuation was calculated using a so-called 'pencil beam' code designed for interpretation of CER data on DIII-D; the code is based around effective stopping cross sections drawn from ADAS databases of full collisional radiative modeling over a wide range of plasma parameters [20, 21]. The vertical neutral profile shown in figure 5(*b*) is what is assumed in TRANSP modeling [17] and will be addressed in more detail later. The local D_α emissivity of full energy neutrals was also drawn from ADAS database lookup tables, namely the *ADF22 BME: effective beam emission coefficients* [24]. Also included was the effect of carbon impurity ions. It should be noted that the ADAS BME tables give an effective beam emissivity (E_{adas}) that is related to the volume D_α emissivity mentioned in section 3.1 by $E_{D\alpha} = E_{adas}\, n_o\, n_e$. E_{adas} has units of (ph cm^3 s^{-1}). The attenuation

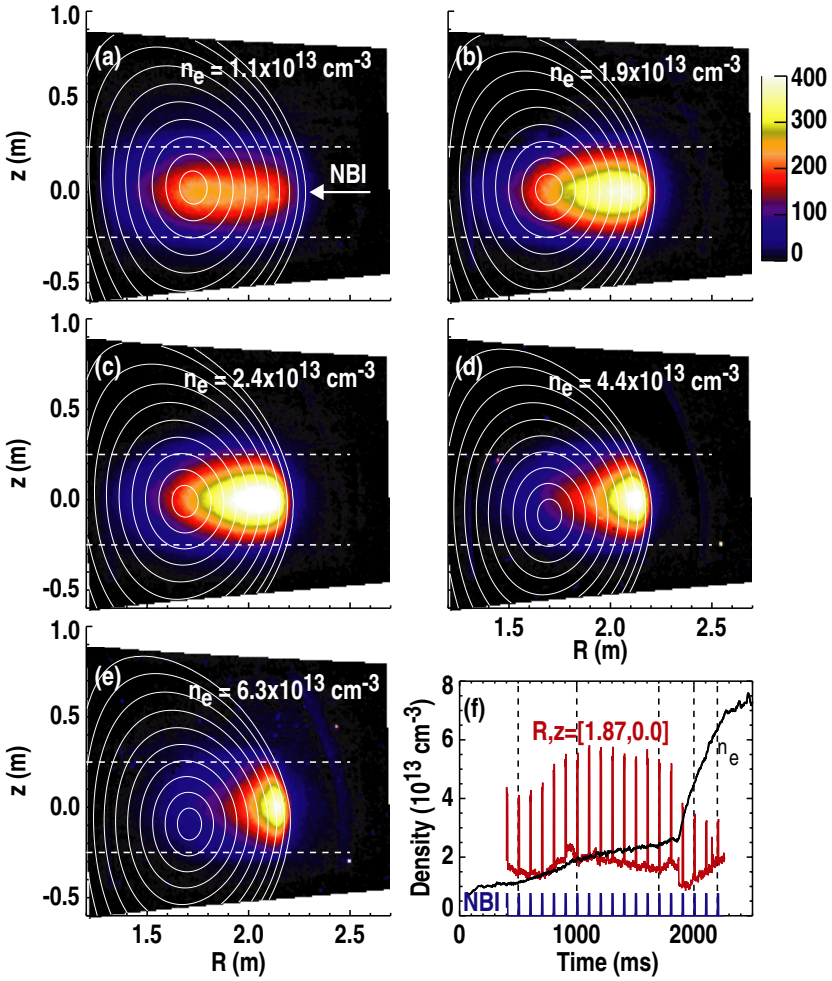

Figure 4. D_α imaging data from DIII-D discharge 135851 showing change in active signal as density rises (*a*) through (*e*). Active signal is isolated through beam modulation as in figure 3. All images are on the same color scale. Corresponding electron density is shown in the upper right corner of each image. R, z coordinates correspond to LOS intersection with 30L neutral beam. Equally spaced contours of $\rho = 0.1$–1.0 evaluated at R, z are overlaid (solid) as well as approximate vertical extent of neutral beam. (*f*) Temporal evolution of line-averaged density (solid black), temporal evolution of pixel at beam intersection $(R, z) = (1.87, 0)$ m (solid red) showing beam modulation (solid blue) of active signal. Vertical dashed lines correspond to times at which panels (*a*)–(*e*) are derived. Camera sampling rate was 900 frames s^{-1} and exposure time was 1.1 ms. $T_i \approx T_e$, which on axis, varies from 1 keV in the lowest density case to 3.7 keV in the highest density case.

factor and local emissivity were calculated for experimentally measured profiles of n_e, T_e, T_i and Z_{eff} in discharge 135851 at $t = 2005$ ms, i.e. the 4.4×10^{13} cm^{-3} case from figure 4(*d*). Figure 5(*d*) shows the combined effect of figures 5(*a*)–(*c*). As expected, this model calculation is very similar to the camera measured D_α images in figures 4(*d*) and 10(*a*).

Having seen that one can reproduce many of the gross features of the D_α images from the camera using local plasma parameters combined with a simple neutral penetration model and lookup tables of effective beam emissivities, we now compare the density variation results

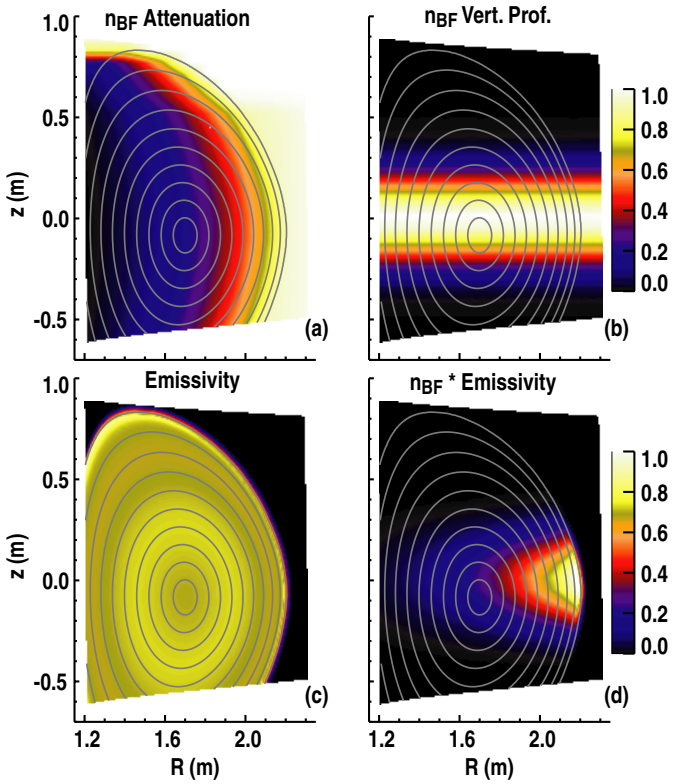

Figure 5. Modeling of the various contributions to injected D_α images. Profiles correspond to discharge 135851, $t = 2005$ ms, the same time as figure 4(*d*). (*a*) Pencil beam neutral penetration code results for attenuation of full energy (40 keV amu^{-1}) deuterium neutrals. Results correspond to vertically uniform beam with no divergence impinging on plasma from LFS. (*b*) Vertical neutral profile from figure 8(*c*) mapped to camera FOV. (*c*) Normalized local full energy deuterium D_α emissivities derived from measured profiles of n_e, T_e and Z_{eff} combined with ADAS beam emissivity lookup tables [20]. (*d*) Combination of all three 2D profiles shown in panels (*a*)–(*c*) which form the full energy contribution to figure 10(*a*).

observed in figure 4. To simulate the actual camera measurements for a given set of plasma parameters, calculations such as that shown in figure 5 are carried out for each energy species, as well as to determine the filter transmission at the expected Doppler-shifted wavelength and distance through the neutral plume across the FOV. The contributions for the three energy components are summed to determine a total surface radiance. To relate the surface radiance values to camera counts, an absolute calibration factor is used which is discussed further in the next section in the context of measurements at ≈529 nm. This factor is related to the calibration at D_α by noting that at the time the measurements are made, the relative sensitivity of the camera/fiber waveguide system is five times higher at 656 nm than at 529 nm. This factor changes in time due to the preferential neutron degradation of the fiber waveguide transmission in the blue. The results of these calculations for pixels that view along the device midplane are shown in figure 6(*a*). For comparison, the camera measurements are given in figure 6(*c*).

The local model appears to capture the behavior with major radius for the five different densities as well as the relative magnitude among the various cases, with the exception that the lowest density case appears too high and too peaked at the edge. This discrepancy could be due to the use of local plasma parameters in determination of the emissivity. In reality, the

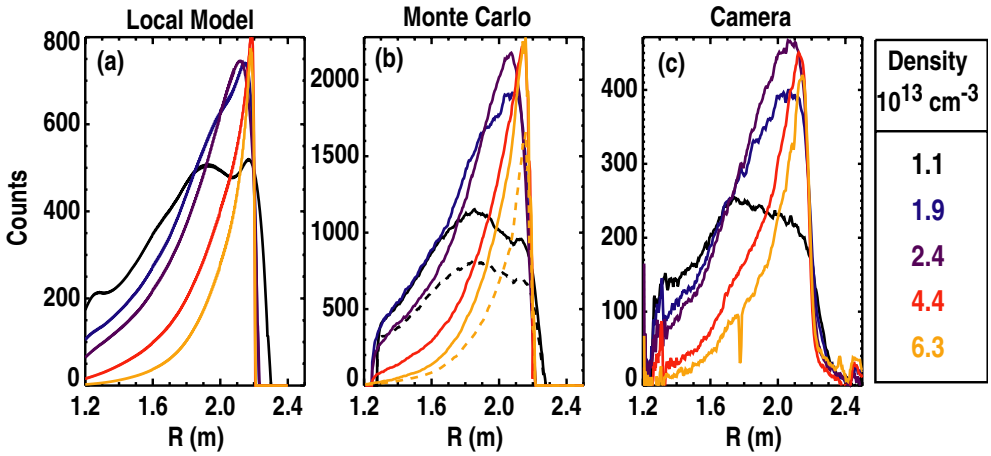

Figure 6. Modeling of midplane active D_α camera measurements along the device midplane for the various density conditions shown in figures 4(*a*)–(*e*). (*a*) Results of local modeling using ADAS beam emissivity lookup tables and pencil beam neutral penetration calculations for the full, half and third energy neutral components based on experimental profiles of n_e, T_e and Z_{eff}. (*b*) Full Monte Carlo collisional radiation modeling calculations which include both beam emission and thermal deuteron charge exchange emission (solid). Dashed curves represent beam emission only for $n_e = 1.1 \times 10^{13}$ cm^{-3} (black) and 6.3×10^{13} cm^{-3} (yellow). (*c*) Camera measurements of active D_α signal with vignetting removed for comparison with (*a*) and (*b*).

neutrals have a finite lifetime and traverse a significant distance before decaying. In regions of sharp gradients, such as at the edge, the consequences of this assumption should be most pronounced. It is not expected, however, that the exact spatial structure will be reproduced with this simple analysis since the contribution of thermal charge exchange signal has been neglected. In terms of absolute signal level comparison, it appears that the predicted values are approximately a factor of two too large, even with the neglected thermal signal. This difference will be addressed after results from more detailed calculations are discussed (figure 6(*b*)).

In addition to the local model calculations, the same input profiles provide input to a collisional radiative modeling code described in [15, 16], which was originally designed for simulation of FIDA data. The code launches Monte Carlo neutrals from the source region and follows them through the beam aperture into the vessel until lost due to ionization or charge exchange while keeping track of state populations. It is capable of calculating the full spectrum of D_α emission from the injected neutrals, including Stark splitting, thermal charge exchange and fast ion re-neutralization, giving the theoretical photon flux observed by each pixel per unit wavelength. Uniformly distributed neutrals are launched from a source with half width dimensions of $W \times H = 6.0 \times 24.0$ cm along paths with normally distributed angles representing a divergence of 0.0227 and 0.00873 rad in the vertical and horizontal directions, respectively. The neutrals are clipped by an aperture of dimensions $W \times H = 8.85 \times 24.0$ cm that is 186.1 cm from the source. The beam is focused in the vertical direction at 10 m from the source and assumed to be essentially parallel in the horizontal direction. Detailed comparisons of the neutral deposition with TRANSP calculations and with pencil beam calculations along the beam centerline have been carried out and reasonable agreement was found [25].

An example theoretical spectrum is given in figure 2 for a midplane sightline which intersects the 30L neutral beam at $R = 2.01$ cm, where $n_e \approx 2 \times 10^{13}$ cm^{-3}, $T_e = 0.5$ keV, $Z_{eff} = 1.2$, for the time of figure 4(*b*). The code has been adapted to take the array of

sightlines for the camera diagnostic as well as to integrate over the appropriate wavelength range for each pixel [5]. Since the full spectrum is calculated, it is straightforward to include the camera bandpass filter transmission properly for each LOS. The theoretical spectra including FIDA emission and thermal charge exchange have been compared in detail with measurements using the DIII-D dedicated FIDA spectrometers [6, 16].

As with the local model, many of the major trends are captured by the Monte Carlo code, in fact, the structure and relative changes with density are all reproduced extremely well. The absolute magnitudes, however, are in even larger disagreement with experiment. This is to be expected for two reasons. First, the inclusion of the thermal charge exchange signal can only increase the magnitude. The relative importance of this emission source is shown in figure 6(*b*) for the lowest and highest density cases, where the simulated camera signals from beam emission only are shown as dashed lines. The thermal charge exchange signal is the difference of the solid and dashed lines. Second, it has been pointed out that the ADAS fractional populations used for the local calculations are approximately a factor of two too low [19] for the plasma conditions here. This appears to be corroborated by comparison of the black and yellow dashed curves in figure 6(*b*) with the solid black and yellow curves of figure 6(*a*).

A regression analysis shows that the simulation is approximately a factor 4.8 larger than that measured, with a reduced chi-squared of 5.6, indicating, as mentioned, that the spatial structure and relative changes with density are well represented by the simulation. At the time of writing, this difference in magnitude is not understood. Almost all conceivable factors would actually enhance the discrepancy. It is pointed out that the beam area is one unknown that is important in calculating the actual edge neutral density from injected power measurements. However, what actually enters the emission measurement calculations is the vertical profile only since the horizontal width dependence cancels when the integration along the LOS is performed. The vertical profile has been measured here to much better than the factor which would be required to resolve this discrepancy. The calculated neutral profile is also intrinsic to calculations of FIDA emission which, when compared with DIII-D's absolutely calibrated FIDA spectrometers, appears to be lacking this large discrepancy [6, 16].

3.3. Extracting beam vertical profile from injected neutral images

The vertical profile of neutrals in the injected beam, such as that shown in figure 5(*b*), can be extracted from imaging data through both injection into plasma as well as neutral gas [26]. We will discuss the case of injection into plasma first and then the more informative case of injection into neutral gas. Figure 7 shows the intensity along various flux surfaces plotted versus z position on the outboard side [$I(z)$]. In a local sense, and neglecting beam divergence, which will be discussed next, $F_3 \approx F_3(\rho)$, and for a *vertically uniform beam*, i.e. $N_s(z) = 1$, the emission should be a flux surface quantity at the outermost flux surfaces on the LFS, where $N_A(R, z) \approx N_A(\rho) \approx 1$; deviations from this yield the vertical neutral profile $N_s(z)$. The local approximation here relies on the fact that the fractional population is dependent on flux surface quantities [$F_3 \approx F_3(\rho)$] and, for a vertically uniform beam, each flux surface on the outboard side is populated with the same density of neutrals. As the neutrals traverse the plasma radially, attenuation becomes significant, the flux surfaces become more circular and the neutral density on the outboard side varies significantly about a flux surface. This can be seen in figure 5(*a*), where $N_A(R, z)$ is essentially the neutral profile in the plasma for a vertically uniform beam and is given for a specific set of plasma parameters. The attenuation versus distance traveled by a neutral from the point at which attenuation begins becomes a function of z owing to different path lengths between flux surfaces. Thus, at outer radii, one

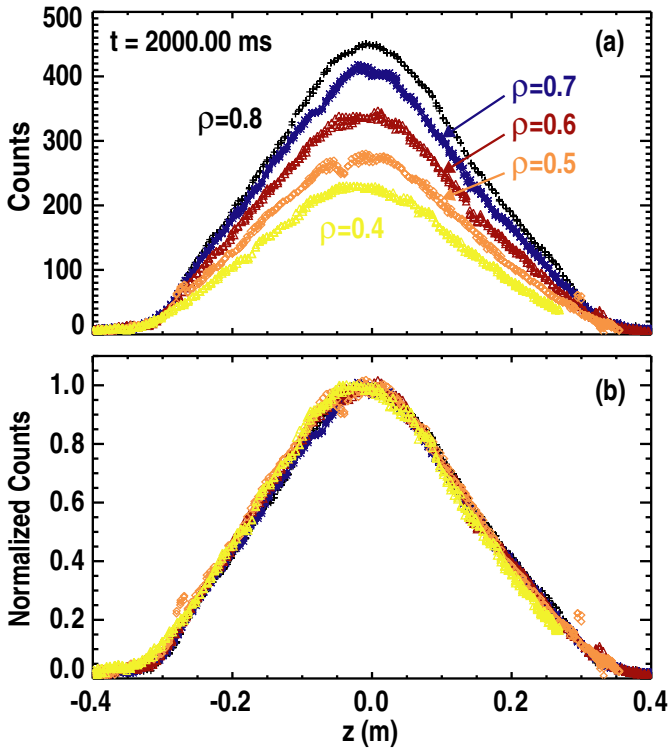

Figure 7. Active D_α signal intensity from discharge 135851 figure 4(*d*). (*a*) Pixel counts along outer flux surfaces at $\rho = 0.4, 0.5, 0.6, 0.7$ and 0.8 in figure 4(*d*) plotted versus z-coordinate between $-0.4\,\mathrm{m} < z < 0.4\,\mathrm{m}$. (*b*) Data from panel (*a*), where each curve from the different ρ values has been normalized to its peak value.

would expect almost a self-similar emission profile, $I(z)$, when plotted for various ρ values. This is what is shown in figure 7(*b*), where the vertical profiles from figure 7(*a*) are normalized to their peak and re-plotted. The profile shown in figure 7(*b*) is a good approximation to the vertical profile of the injected neutrals, where a similar shape must be assumed for the full, half, and third energy components.

As a second measure of the vertical profile of neutrals, and one which now yields the overall beam divergence, neutral deuterium injection into neutral helium gas was carried out. Spectroscopically, injection into neutral helium eliminates emission from all other sources in the filter passband except for Doppler-shifted D_α from the beam neutrals excited by collisions with the helium. The results from injection into neutral helium are given in figure 8, where the raw image data during a 50 ms long beam blip of the 30L source are shown in panel 8(*a*). Figure 8(*b*) shows the data from figure 8(*a*) re-plotted with the camera vignetting removed and with each vertical profile normalized to its peak value. The beam vertical profile derived from figure 8(*b*) is shown for two different major radii in figure 8(*c*). Overplotted is a fit to the vertical beam emission profile in figure 7(*b*) (solid green line) as well as the assumed profile of full energy neutrals near $R = 2.2$ m used for all DIII-D TRANSP [17] modeling (dashed line). The good agreement with the TRANSP injected neutral profile is fortunate, since a difference would have had major implications for all historical TRANSP analysis of DIII-D discharges. The level of agreement is also somewhat remarkable considering that the vertical profile used in

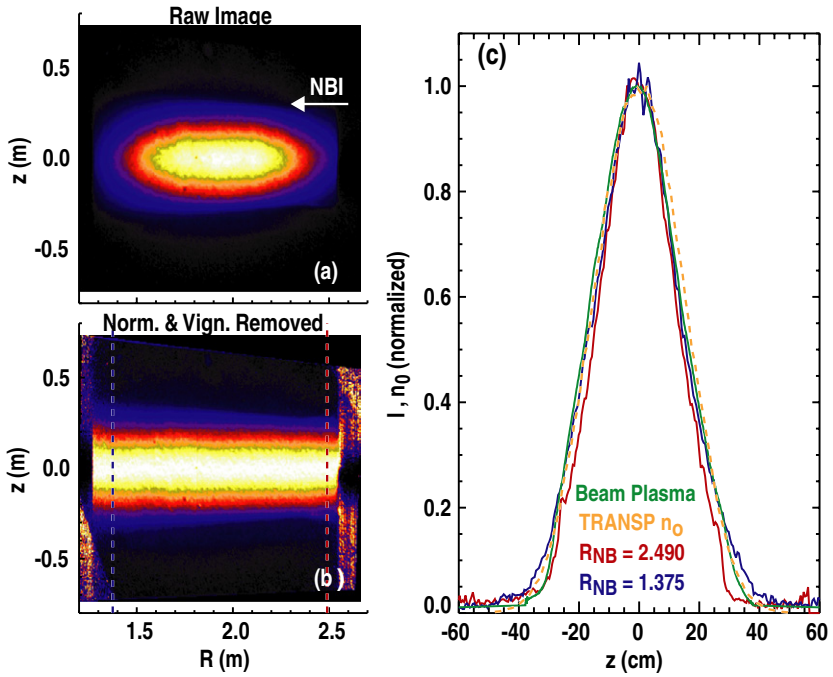

Figure 8. Active red-shifted D_α data for deuterium beam injection into chamber filled with neutral helium gas. (*a*) Raw image, which includes camera vignetting and variation of filter transmission function across FOV. (*b*) Image from panel (*a*) with camera vignetting removed and each vertical pixel column normalized to the peak value in that column. (*c*) Image data from panel (*b*) where data are plotted versus z-coordinate to show vertical neutral brightness profile at the LOS beam intersection radii of $R_{\rm NB} = 2.490$ and $R_{\rm NB} = 1.375$, red and blue, respectively. Dashed vertical lines in panel (*b*) show major radii at which beam into gas data are plotted in (*c*). Solid green curve is the vertical brightness profile shown in figure 7(*b*) derived from beam injection into plasma. Dashed orange curve is vertical profile of neutral density for the full energy component ($n_{\rm o}$) at $R = 2.02$ m from a TRANSP [17] simulation.

TRANSP was derived from the backprojection of four calorimeter measurements on the inner wall for a different beam source [21]. For reference, the TRANSP profile is well approximated by $n_{\rm b}(z) \approx {\rm e}^{-(z/21.1)^2}$, where z is the vertical position in centimeters.

The beam into gas measurements shown in figure 8 yield two interesting results beyond the overall shape and width of the vertical neutral profile. First, at large radii, the vertical neutral profile appears to be clipped at vertical positions outside of $|z| \approx 26$ cm. This is presumably a result of the beam shaping collimators in the source. At smaller major radii, the beam is well described by a Gaussian. Second, the overall vertical width variation with distance traveled along the beam is obvious and gives a measure of the beam divergence.

The vertical beam half-width-half-max (HWHM) as a function of distance along the beam (D) is shown in figure 9, where the results of two different techniques are given. Here, $D = 0$ corresponds to $R_{\rm NB} = 2.513$ m. The technique labeled 'Gaussian fit' (red) is from the fitting of a Gaussian to the vertical emission profile at each major radius. The technique labeled 'from raw data' (blue) is simply finding the points above and below the centerline at which the intensity shown in figure 8(*b*) is 0.5 at each major radius. The Gaussian technique has an implicit assumption of symmetry of the emission profile about some point on the z direction, while the 'raw data' technique relies on some smoothing interval to normalize

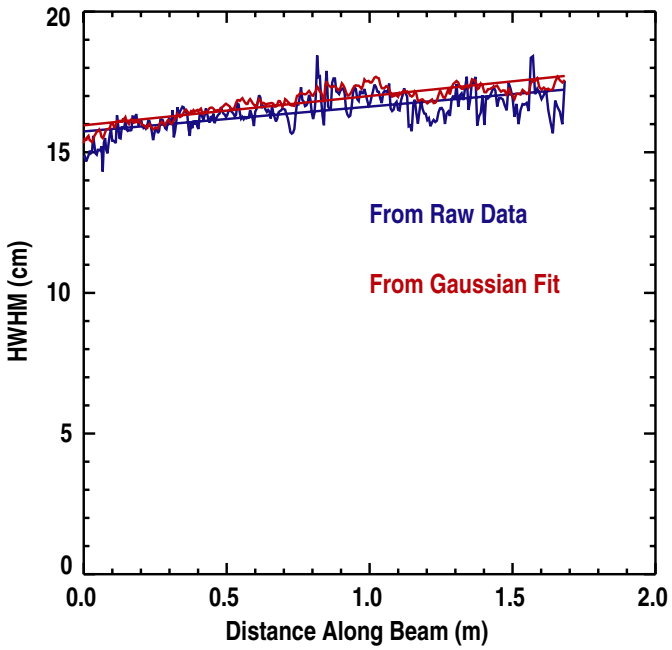

Figure 9. Active red-shifted D_α data for deuterium beam injection into chamber filled with neutral helium gas. FWHM of beam vertical profile versus distance (D) along beam. $D = 0$ is at $R_{\mathrm{NB}} = 2.513$ m. Raw data FWHM values and Gaussian fit FWHM values are the noisy blue and red curves, respectively. Line fit values are the smooth lines.

the intensity. Despite these differences, both techniques give very nearly the same HWHM values as well as divergences. The calculated HWHM divergences are $\alpha = 0.60 \pm 0.02^\circ$ and $\alpha = 0.51 \pm 0.03^\circ$ for the Gaussian and 'raw data' approaches, respectively. Line fits to the HWHM yield HWHM $= 1.042D + 15.96$ and HWHM $= 0.883D + 15.74$ for the Gaussian and 'raw data' approaches, respectively, where D is in meters and the HWHM values are in centimeters.

Now that the source-imposed, vertical profile of injected neutrals $[N_{\mathrm{s}}(z)]$ is known, we can utilize this information and normalize it out of the beam images, i.e. we will plot $I/N_{\mathrm{s}}(z)$. This is shown in figure 10(b), where the data from figure 4(d) have been used and figure 10(a) is a smaller region of figure 4(d) with the effects of camera vignetting removed. Each pixel value in figure 10(b) has been normalized by the corresponding beam profile at that z location. The plotted range has been restricted in z; outside of this range the signal levels are bit level so division by the vertical beam profile results in an enhancement of what is essentially noise. Immediately obvious from figure 10(b) is that the emission boundary on the outboard side closely follows the shape of the LCFS. At smaller radii this is approximately the case on the outboard half of each flux surface. Again, as mentioned above, it is expected that deviations to this will come from the fact that the injected neutral density varies slightly as one traverses the flux surface. Because the emissivity is relatively constant across the FOV, figure 10(b) looks very similar to the 2D profile of neutral attenuation between $-0.25\,\mathrm{m} < z < 0.35\,\mathrm{m}$ shown in figures 5(a).

Imaging of the outboard flux surfaces as shown in figure 10(b) could potentially be useful to future devices such as ITER where the plasma position must be known accurately and

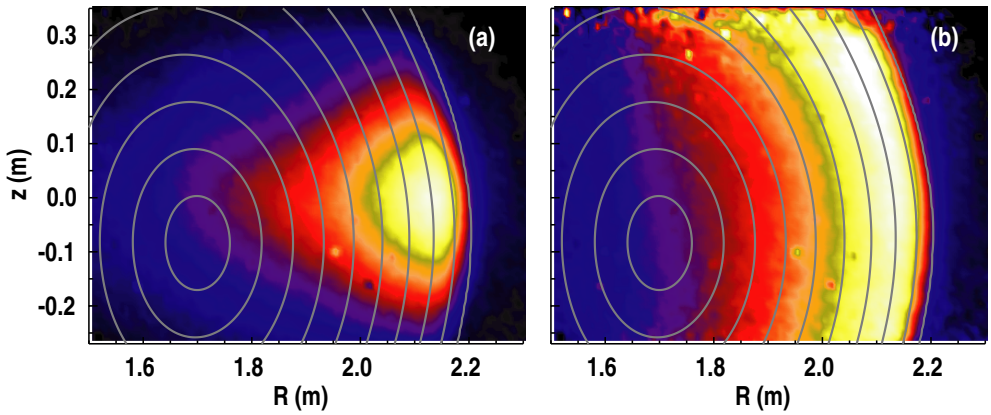

Figure 10. (*a*) Data from figure 4(*d*) with camera vignetting removed. (*b*) Data from panel (*a*) with vertical beam profile removed. Removal was accomplished by interpolating $I(z)$ from figure 8(*c*) to each pixel's vertical location and dividing intensity by corresponding value. Equally spaced contours of $\rho = 0.1$–1.0 are overlaid.

diagnostics beyond magnetics will be required. Currently, a reflectometer system is planned to provide a reference for the magnetic diagnostics in long pulse discharges [27].

3.4. Carbon impurity imaging

Active beam imaging opens many diagnostic possibilities. From the perspective of ease of implementation, particularly attractive are ones which require little spectral resolution, such as the measurement of impurity densities via CER. In DIII-D, CER is used to monitor C VI impurity ion density, temperature and toroidal rotation by active spectrometer-based measurement of the 529.05 nm CER line [28–31]. C VI density is derived from the total brightness of the C VI CER line combined with the local neutral density of each of the full, half and third energy components and the appropriate cross section for charge exchange between fully stripped carbon on each energy component. The neutral penetration (which depends on the impurity density) is calculated by an iterative procedure. Since the measurement of impurity density relies on only the total brightness of the C VI CER line, an equivalent 2D measurement can be implemented with the same imaging techniques mentioned in the previous section by replacing the D_α filter with a narrowband bandpass interference filter designed to pass the 529.05 nm line.

Figure 11 shows a typical CER spectrum measured during 30L beam modulation, where data with and without the active neutral source are given. It is thought that some level of the C VI CER emission is observed even without the injected source of neutrals, due to the fact that the carbon tiles can provide a source of cold neutrals at the edge. The peak in the spectrum in the 'BEAM OFF' curve (blue) is slightly shifted relative to that in the 'BEAM ON' case. The shift is due to plasma rotation and one subtlety associated with these data is that the clockwise viewing geometry dictates that the CER spectrometer view measures an opposite Doppler shift relative to the counter-clockwise view of the camera. The bandpass filter transmission profile used for C VI measurements is shown overlaid in figure 11 along with an additional filter used specifically for visible bremsstrahlung measurements which will be discussed in section 4. The C VI passband was chosen taking into account the blue shift of the transmission profile resulting from the variation of the angle of incidence on the filter across the FOV, the Doppler shift of the line for typical rotation velocities and broadening of the line due to finite temperature.

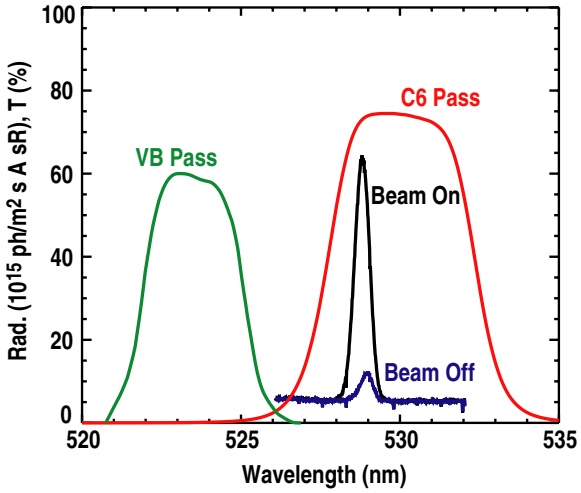

Figure 11. Spectrum from discharge 135847 showing C VI charge exchange line at 529.05 nm measured using CER spectrometer with ('beam on') and without ('beam off') 30L neutral beam on. Spectrometer intersects 30L beam at $(R, z) = (2.08, 0.00)$. Spectrum baseline level is primarily due to VB. Transmission functions of bandpass filters used for C VI CER and VB measurements are also shown.

Data taken with the C VI filter in place are given in figure 12. Figure 12(*a*) shows the temporal evolution of a midplane camera pixel viewing at approximately mid-radius on the outboard side of the magnetic axis. For reference, the 30L neutral beam modulation waveform is also given. One can see a clear signal enhancement when the neutral source is on due to the active charge exchange signal. The level of this enhancement changes drastically across the FOV as well as in time due to variation in the impurity profile and in the neutral penetration. The baseline level, observed during beam off phases, contains some contribution from the edge induced C VI emission as well as from VB. Figure 12(*b*) shows the active signal only, from camera measurements (solid line) and from the spectrometer-based CER system (diamonds). The camera pixels plotted were chosen to correspond to the same beam intersection locations as the spectrometer views. As expected, the camera system is able to accurately reproduce the temporal evolution and structure of the C VI emission derived from DIII-D's CER diagnostic.

The radial profile of the C VI emission from both diagnostic techniques is shown more clearly in figure 13(*a*) for three different times, where it is seen that the camera measurements (solid line) reproduce well the CER spectrometer measured profiles (diamonds). Of course, one of the benefits of the camera based system is the extremely fine spatial resolution obtainable. An example of this is given in figure 13(*b*), where the 2D profile of C VI emission is shown for the $t = 2400$ ms case. Figure 13(*b*) has the effects of camera vignetting removed as well as that of the vertical neutral profile. Actual 2D impurity densities can be obtained from images such as figure 13(*b*) in the same iterative manner as used for traditional radial CER spectrometer profiles, i.e. an impurity density profile is assumed, neutral penetration is calculated, an impurity density profile is then calculated using this neutral population based on the measured emissivities and cross sections and the loop is iterated.

Also included in figures 12 and 13 is an absolute scaling for the camera system. These surface radiance magnitudes were derived by scaling the camera data using a single constant to match the spatial and temporal evolution of the absolutely calibrated CER spectrometer array measurements. The possibility of obtaining an absolute scaling from CER measurements is an

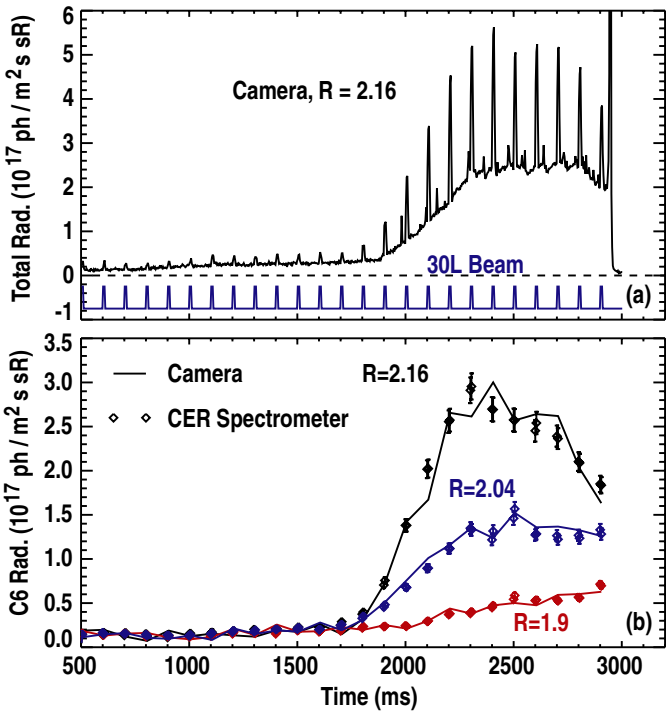

Figure 12. Discharge 135847 imaging data taken with C VI filter shown in figure 11, and camera frame rate of 300 frames s^{-1}. (*a*) Raw camera signal for pixel with beam intersection location $(R, z) = (2.16, 0.0)$ m shown in black. Beam modulation waveform shown in blue. (*b*) Temporal evolution of active camera signal (obtained by removal of beam-off non-active signal) for three different midplane radial locations. Diamonds indicate CER spectrometer measured C VI brightness at same intersection locations. All camera data scaled by single constant to match CER data and obtain absolute calibration at 529 nm—same scaling constant was used to give absolute surface radiance values in panel (*a*).

extremely useful result since the absolute camera calibration can change on day and certainly week time scales due to neutron induced degradation of the fiber waveguide transmission.

4. Passive imaging—bremsstrahlung

In addition to imaging active sources, which require a source of injected neutrals, passive measurements are possible. In the visible region, the primary source of passive emission is bremsstrahlung. The local bremsstrahlung emissivity (N_B) per unit wavelength is given by

$$\frac{dN_B}{d\lambda} = 7.57 \times 10^{-9} g \frac{n_e^2 Z_{eff}}{\lambda\, T_e^{1/2}} e^{-hc/\lambda T_e}, \tag{2}$$

where λ is the wavelength in angstroms, n_e is the electron density in (cm^{-3}), T_e is the electron temperature in (eV) and $dN_B/d\lambda$ has units of photons $(m^3\ \text{Å}\ s\ sr)^{-1}$. The Gaunt factor, g, in equation (2) depends on T_e and Z_{eff}; it may be approximated by

$$g = 5.542 - [3.108 - \ln(T_e/1000)](0.6905 - 0.1323/Z_{eff}), \tag{3}$$

where the scaling was derived from a fit [33] to calculations based on the original work presented in [32]. The algebraic dependence on T_e and Z_{eff} replaces a constant factor of 3 used in [2].

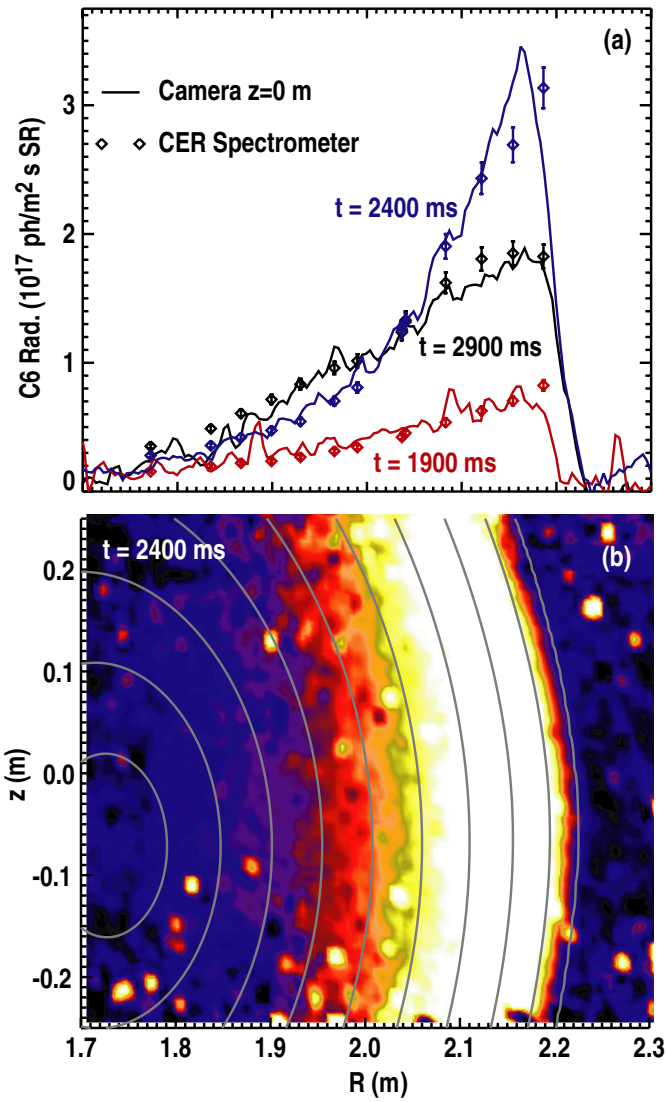

Figure 13. Discharge 135847. (*a*) Radial profile of active C VI CER signal from camera (solid) and CER spectrometer (diamonds) at $t = 1900$, 2400 and 2900 ms. (*b*) 2D image of C VI emission at $t = 2400$ ms. Vignetting and vertical neutral profile have been removed. Equally spaced flux contours for $\rho = 0.1$–1.0 are overlaid.

Camera measurements of bremsstrahlung have been made previously [1–3]; the bremsstrahlung continuum is always present as a background underlying active measurements and is particularly obvious during the beam-off phase [5]. The filter used here to obtain VB measurements has the identical bandpass as the calibrated VB array which views the tangential midplane of DIII-D [34]. Its transmission function is shown in figure 11. The ≈3 nm transmission passband centered at 523 nm was chosen to isolate a narrow, relatively line-free region; and is within 6 nm of the nominal C VI charge exchange line.

Camera measurements of the bremsstrahlung emissivity are shown in figure 14. In figure 14(*a*) the 2D data are plotted versus major radius and height at the point where each

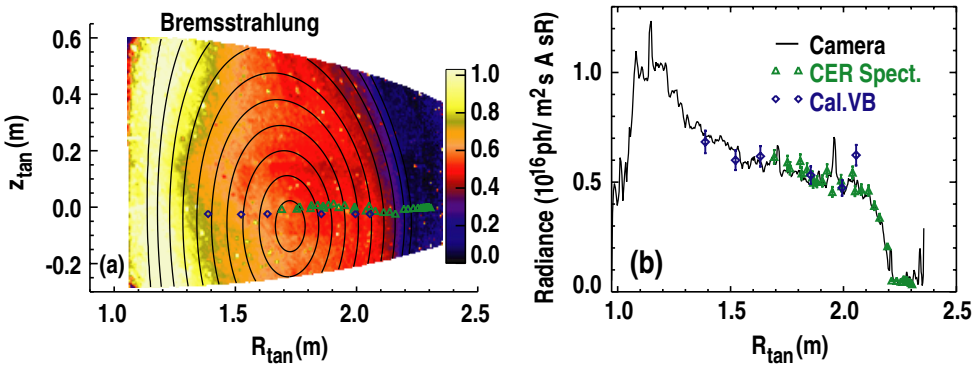

Figure 14. VB data from discharge 135845. (*a*) 2D camera image with vignetting removed. Line-free region of bremsstrahlung was isolated using 523 nm filter shown in figure 11. Overplotted diamonds/triangles indicate calibrated VB array and CER spectrometer tangency locations. (*b*) Midplane radial profile of VB surface radiance derived from camera, VB array and CER spectrometer.

sightline is tangent, $R_{\tan}$ and $z_{\tan}$, respectively. Overplotted are contours of ρ mapped to the point of tangency. The bremsstrahlung signal detected by the camera has been corrected to remove the vignetting function. Overplotted on the 2D image in figure 14(*a*) are the sightline locations of the VB calibrated array (diamonds) and the CER spectrometer (triangles). Note that the CER spectrometer is an equally useful *passive* bremsstrahlung diagnostic, since the entire spectrum is recorded at each location and the baseline level is a measure of the bremsstrahlung emission [35]. An example of bremsstrahlung measured by the CER system can be seen in figure 11, where the prominent CER peak sits atop a relatively flat continuum of emission with an amplitude of approximately 5×10^{15} ph (m^{2}s A sr)$^{-1}$. As shown in figure 11, the continuum does not change with beam modulation. A comparison of the midplane VB profile measured by the camera, CER, and VB array is given in figure 14(*b*); the shape and absolute magnitude agree well among the three.

Unlike active measurements for which the column-integration of light is limited to the path length through the neutral plume, VB measurements are column-integrated along the entire length of the sightline through the plasma column. With so many channels, however, the data can be successfully inverted in a number of ways to obtain measurements of the local emissivity profile. Midplane data, such as that presented in figure 14(*b*), can be inverted using the assumption of toroidal symmetry and a straightforward Abel inversion [36]. Abel inversion techniques, however, are very sensitive to noise and limit the use of the 2D camera data to just the midplane pixels. Instead, a different approach has been focused on, which assumes the local emissivity to be a flux function described by some spline function with an arbitrary number of knots and arbitrary placing. Line integrals are taken through the profile along each camera pixel's sightline and through a straightforward minimization procedure, the shape of the local emissivity is arrived at. The exact minimization algorithm used is the same as that used for fitting of all other DIII-D profiles such as n_e, T_e and T_i, etc.

The various components of this inversion process are shown in the four panels of figure 15. The line-integrated VB emission measured by the camera is shown in figure 15(*a*), the simulated line-integrated emission in figure 15(*b*), the corresponding 2D local emissivity contour in figure 15(*c*) and derived emissivity profile versus ρ is figure 15(*d*). One of the reasons to measure VB emissivity is to obtain a check on the separate profiles of n_e, T_e and Z_{eff} measured by other diagnostics. A comparison of the local emissivity profile derived from camera data

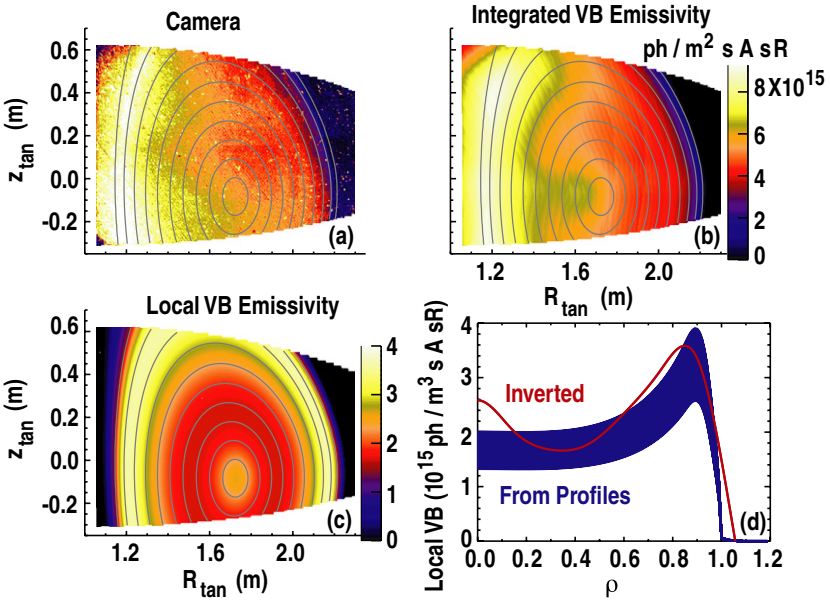

Figure 15. (*a*) Camera measured VB emission from discharge 135845, $t = 2505$ ms. (*b*) Line-integrated fit to camera data using local VB emissivity shown in panel (*c*). (*d*) Local VB emissivity versus ρ derived from inversion of camera data and that from measured profiles of n_e, T_e and Z_{eff}, labeled 'inverted' and 'from profiles', respectively. Local emissivity evaluated according to equation (2).

with that calculated from the measured local profiles of n_e, T_e and Z_{eff} is given in figure 15(*d*). The width of the emissivity curve calculated based on local profiles reflects the uncertainty derived from errors in the measurement of each underlying profile. While the two emissivity profiles are similar, this comparison suggests that the measured local profiles have either too low n_e or Z_{eff} in the core and edge or T_e is too high. Since the local bremsstrahlung emissivity depends sensitively on electron density ($\propto n_e^2$), the comparison is a good check on the magnitude of electron density. Similarly, given an electron density and electron temperature measurement (which do not require a diagnostic beam), one can use the camera data to obtain Z_{eff} in plasmas, even without active CER measurements [1, 29, 34].

As mentioned earlier, the analysis shown in figure 15 assumes that the emissivity is a flux function, something which may not be the case, particularly in plasmas with large rotation velocities where the centrifugal force on impurities can be significant. A poloidally dependent emissivity profile would be more appropriate for that case and could be incorporated into the inversion routines to take full advantage of the wide FOV images. Note that Abel inversion of the midplane data alone does not require the local emissivity to be a flux function; however, Abel inversion would only yield the inboard/outboard asymmetry and not the full poloidal dependence.

5. Summary, conclusions and future

In summary, wide-angle 2D imaging of Doppler-shifted D_α emission from high energy injected neutrals, CER emission from neutralized C VI ions and VB from the core of DIII-D plasmas has been presented. Measurements of the D_α emission from injected neutrals reveal the full

2D structure of the injected beam, its divergence and the 2D attenuation variation with density. Modeling of this emission using both a full Monte Carlo collisional radiative code [15, 16] as well as a simple beam attenuation code coupled to ADAS emissivity lookup tables yields qualitative agreement, however the absolute magnitudes of the emissivities in the predicted distribution are larger than those measured. Measurements of impurity CER brightness are in agreement with those made independently using DIII-D's standard CER spectrometer array, showing the potential of this technique for obtaining 2D impurity density profiles. Passive imaging of VB was also discussed and a favorable comparison with both a calibrated photodetector array and spectrometer array was made. The obtained VB images were inverted to obtain local emissivity profiles.

The measurements presented here represent only a few examples of what is now technically possible using deep-memory fast-framing cameras with large dynamic range. These CMOS devices offer virtually unlimited potential for high spatial resolution plasma diagnostic applications. Indeed, more elaborate active imaging applications are on the horizon. One example, already under development [37], is the use of polarization information encoded in the beam emission to create an imaging motional Stark effect (MSE) system. Particularly exciting is that wide-angle imaging of beam emission with a fast-framing camera, such as that presented in section 3.1, opens up the possibility of a 2D fluctuation diagnostic [13] similar to the individual detector-based BES system on DIII-D [38]. Instead of 64 pixels of the present BES system, however, a camera version could easily have up to 10^4 pixels; the addition of an image intensifier and greater bit-depth camera would make such a system even more feasible.

The same techniques as presented here could be applied on future tokamaks equipped with imaging ports, such as ITER. For example, imaging of the outboard flux surfaces, as shown in figure 10(*b*), could be used to supplement the position control and equilibrium reconstructions on long pulse discharges where magnetic diagnostics will need a reference [27]. In fact, the future of imaging applications may be even more encouraging than depicted by this work. On the timescale of a decade, the fast-framing camera technology of today may be supplanted by high density large gain, extremely large bandwidth APD or p–i–n photodiode arrays currently being developed for 3D imaging applications [39–41]. These detectors have single photon counting capability, adjustable gain and function easily with bandwidths in the 100 MHz through 1 GHz range.

Acknowledgments

This work was supported by the US Department of Energy under DE-FC02-04ER54698, DE-FG02-07ER54917, SC-G903402 and DE-AC02-09CH11466. The authors would like to thank the DIII-D team for providing the plasmas and specially acknowledge Dr Martin O'Mullane's help with the ADAS database analysis and Dr Brian Grierson's careful analysis of the FIDA simulation code. Effective beam emissivities, stopping cross sections and charge exchange cross sections in the FIDA simulation code were obtained from the Atomic Data and Analysis Structure (ADAS) compilation. The originating developer of ADAS is the JET Joint Undertaking.

References

[1] Patel A, Carolan P G, Conway N J and Akers R J 2004 *Rev. Sci. Instrum.* **75** 4944
[2] Van Zeeland M A *et al* 2008 *Nucl. Fusion* **48** 092002
[3] Yu J H and Van Zeeland M A 2008 *Rev. Sci. Instrum.* **79** 10F516
[4] Yu J H, Van Zeeland M A, Chu M S, Izzo V A and La Haye R J 2009 *Phys. Plasmas* **16** 056114

[5] Van Zeeland M A, Heidbrink W W and Yu J H 2009 *Plasma Phys. Control. Fusion* **51** 055001
[6] Heidbrink W W *et al* 2009 *Plasma Phys. Control. Fusion* **51** 125001
[7] Howard J *et al* 2003 *Rev. Sci. Instrum.* **74** 2060
[8] Chung J, Konig R, Howard J, Otte M and Klinger T 2005 *Plasma Phys. Control. Fusion* **47** 919
[9] Howard J 2006 *Rev. Sci. Instrum.* **77** 10F111
[10] Howard J and Hatae T 2008 *Rev. Sci. Instrum.* **79** 10E704
[11] Mandl W, Wolf R, von Hellermann M G and Summers H P 1993 *Plasma Phys. Control. Fusion* **35** 1373
[12] Fonck R J, Duperrex P A and Paul S F 1990 *Rev. Sci. Instrum.* **61** 3487
[13] Thomas D M 1996 *IEEE Trans. Plasma Science* **24** 27
[14] Yu J H *et al* 2008 *Phys. Plasmas* **15** 032504
[15] Heidbrink W W, Burrell K H, Luo Y, Pablant N A and Ruskov E 2004 *Plasma Phys. Control. Fusion* **46** 1855
[16] Luo Y, Heidbrink W W, Burrell K H, Ruskov E and Solomon W M 2007 *Phys. Plasmas* **14** 112503
[17] http://w3.pppl.gov/transp/
[18] Janev R K, Boley C D and Post D E 1989 *Nucl. Fusion* **29** 2125
[19] Hutchinson I H 2002 *Plasma Phys. Control. Fusion* **44** 71
[20] Atomic Data and Analysis Structure (ADAS) compilation *ADAS* http://adas.phys.strath.ac.uk
[21] Finkenthal Daniel F 1994 *PhD Thesis* University of California at Berkeley
[22] Pablant N A, Burrell K H, Groebner R J, Kaplan D H and Holcomb C T 2008 *Rev. Sci. Instrum.* **79** 10F517
[23] Dr Grierson B 2009 Private Conversation
[24] Atomic Data and Analysis Structure (ADAS) compilation *ADAS* http://open.adas.ac.uk/adf22.php
[25] Lin Deyong 2009 *PhD Thesis* University of California at Irvine
[26] Hill D N, Allen S L and Pincosy P A 1986 *Rev. Sci. Instrum.* **57** 2069
[27] Vayakis G *et al* 2006 *Nucl. Fusion* **46** S836
[28] Seraydarian Raymond P and Burrell Keith H 1986 *Rev. Sci. Instrum.* **57** 2012
[29] Whyte D G *et al* 1998 *Nucl. Fusion* **38** 387
[30] Burrell K H, Kaplan D H, Gohil, Nilson D G, Groebner R J and Thomas D M 2001 *Rev. Sci. Instrum.* **72** 1028
[31] Wade M R *et al* 2005 *Phys. Plasmas* **12** 056120
[32] Karzas and Latter 1961 *Astrophys. J. Suppl. Ser.* **6** 213
[33] Burrell K H 2009 Private Communication
[34] Schissel D P, Stockdale R E, St John H E and Tang W M 1988 *Phys. Fluids* **31** 3738
[35] Meister H *et al* 2004 *Rev. Sci. Instrum.* **75** 4097
[36] Jackson S L and Shumlak U 2006 *Rev. Sci. Instrum.* **77** 083502
[37] Howard J 2008 *Plasma Phys. Control. Fusion* **50** 125003
[38] McKee G *et al* 1999 *Rev. Sci. Instrum.* **70** 913
[39] Vaidyanathan M *et al* 2004 *Proc. IEEE Aerospace Conf.* **3** 1781
[40] Franco D S *et al* 2005 *Photon. Technol. Lett., IEEE* **17** 873
[41] Nick B and William C 2007 *Laser Focus World* **43** 9